Cement and Concrete Research 41 (2011) 467–476

Contents lists available at ScienceDirect

Cement and Concrete Research

journal homepage: http://ees.elsevier.com/CEMCON/default.asp

Upscaling quasi-brittle strength of cement paste and mortar: A multi-scale engineering mechanics model

Bernhard Pichler *, Christian Hellmich

Institute for Mechanics of Materials and Structures, Vienna University of Technology (TU Wien), Karlsplatz 13/202, A-1040 Vienna, Austria

ARTICLE INFO

Article history:
Received 24 August 2010
Accepted 12 January 2011

Keywords:
Compressive strength (C)
Elastic moduli (C)
Micromechanics (C)
Cement paste (D)
Mortar (E)

ABSTRACT

It is well known from experiments that the uniaxial compressive strength of cementitious materials depends linearly on the degree of hydration, once a critical hydration degree has been surpassed. It is less known about the microstructural material characteristics which drive this dependence, nor about the nature of the hydration degree–strength relationship before the aforementioned critical hydration degree is reached. In order to elucidate the latter issues, we here present a micromechanical explanation for the hydration degree–strength relationships of cement pastes and mortars covering a large range of compositions: Therefore, we envision, at a scale of fifteen to twenty microns, a hydrate foam (comprising spherical water and air phases, as well as needle-shaped hydrate phases oriented isotropically in all space directions), which, at a higher scale of several hundred microns, acts as a contiguous matrix in which cement grains are embedded as spherical clinker inclusions. Mortar is represented as a contiguous cement paste matrix with spherical sand grain inclusions. Failure of the most unfavorably stressed hydrate phase is associated with overall (quasi-brittle) failure of cement paste or mortar. After careful experimental validation, our modeling approach strongly suggests that it is the mixture- and hydration degree-dependent load transfer of overall, material sample-related, uniaxial compressive stress states down to deviatoric stress peaks within the hydrate phases triggering local failure, which determines the first nonlinear, and then linear dependence of quasi-brittle strength of cementitious materials on the degree of hydration.

1. Introduction

Cement paste is the binder for cementitious materials, including cement mortar, concrete, shotcrete, and soilcrete. Therefore, a reliable prediction of mechanical properties of cement paste is paramount for subsequent modeling activities, be they related to material behavior of cementitious composites or to the structural behavior of engineering constructions built up from these materials. Challenging applications even require modeling of the evolution of mechanical properties of *hydrating* cementitious materials. This is e.g. the case for drill and blast tunneling according to the principles of the New Austrian Tunneling Method (NATM), where shotcrete tunnel shells are loaded by the inward moving rock, while the material still exhibits rather small maturities and undergoes the chemical hydration process. This provides the motivation for the present contribution which focuses on upscaling elasticity and strength of hydrating cement paste and mortar, by means of continuum micromechanics.

Within cement paste, hydration products (also called hydrates) establish the links that lead to a network of connected particles. The hydrates' non-spherical phase shape (evidenced by microscopic [1–11] and neutron scattering [12] studies) has been recently shown to probably play an important role in micromechanics-based prediction of the quasi-brittle strength evolution of cementitious materials [13,14]. Thereby, hydration degrees have been estimated from elasticity measurements by means of a (validated) microelastic model, and corresponding measured strength values could be successfully predicted by a microelastic-brittle model with the hydration degrees as input. In this context, a mixture-invariant deviatoric hydrate strength was back-calculated. Having, in this way, gained confidence into the modeling approach, we here aim at a much stricter experimental model test: We wish to predict directly measured hydration-degree–strength relationships for different mixtures, with possibly avoiding any back-calculated strength values. Accordingly, the manuscript is structured as follows:

Section 2 recalls fundamentals of continuum micromechanics. In Section 3, we introduce a micromechanical representation of cement paste and mortar (Section 3.1), followed by corresponding mathematical expressions for upscaling elasticity (Section 3.2) and quasi-brittle strength (Section 3.3). Subsequently, we discuss model input values (Section 3.4). Therefore, we consider dense hydrate foams with very low porosity, from which we identify elastic properties that are, on average, representative for all hydration products. On this basis, our micromechanics models predict elasticity and strength of cement pastes and mortars as functions (i) of hydration degree and (ii) of

* Corresponding author. Tel.: +43 1 58801 20224; fax: +43 1 58801 9 20224.
E-mail address: Bernhard.Pichler@tuwien.ac.at (B. Pichler).

0008-8846/$ – see front matter © 2011 Elsevier Ltd. All rights reserved.
doi:10.1016/j.cemconres.2011.01.010

composition in terms of water-to-cement and sand-to-cement mass ratios (Section 3.5). Section 4 is devoted to model validation, based on the landmark experiments of Taplin [15] who measured early-age strength evolutions of hydrating cement pastes with water-to-cement mass ratios ranging from 0.157 to 0.8, as well as on the equivalence in strength evolutions of standard mortar defined in EN 196-1 [16] and of stoichiometric cement paste. In Section 5, we highlight general model characteristics related to uniaxial compressive strength of cement paste, as a function of the water-to-cement mass ratio and the hydration degree. Finally, we compare our elasto-brittle upscaling scheme with recently published ductile schemes related to the upscaling of confined hardness measurements on cement pastes and concretes (Section 6). This includes an estimate for the shear strength of hydrates.

2. Fundamentals of continuum micromechanics

2.1. Representative volume elements and separation of scales principle

In continuum micromechanics [17–20], a material is understood as a macro-homogeneous, but micro-heterogeneous body filling a representative volume element (RVE) with characteristic length ℓ. The separation of scales requirement implies (i) $\ell \gg d$, where d is standing for the characteristic length of inhomogeneities within the RVE, and (ii) $\ell \ll \mathcal{D}$, where $\mathcal{D}$ stands for the characteristic lengths of dimensions or loading of a structure built up by the material defined on the RVE. Notably, "much smaller ($\ll$)" does not necessarily imply more than a factor of 4 to 5 between the characteristic length of the heterogeneities and that of the RVE [21].

In general, the microstructure within one RVE cannot be described in complete detail. Therefore, quasi-homogeneous subdomains with known physical quantities (such as volume fractions or elastic properties) are identified. They are called material phases. Once their mechanical behavior, their dosages within the RVE, their characteristic shapes, and the mode of their interactions are identified, the "homogenized" mechanical behavior of the overall material can be estimated, i.e. the relation between homogeneous deformations acting on the boundary of the RVE and resulting (average) stresses, or the ultimate stresses sustainable by the RVE, respectively.

In the framework of multiscale homogenization theory, a material phase, identified at a specific scale of observation "A", exhibits a heterogeneous microstructure on a lower scale of observation "B". The mechanical behavior of this microheterogeneous phase can be estimated by that of an RVE with a characteristic length being smaller than *or equal to* the characteristic length of the aforementioned phase, i.e. that of inhomogeneities identified on observation scale "A", see, e.g. [22].

2.2. Field equations and boundary conditions

Within the volume Ω of an RVE, we consider field equations of linear elasticity, i.e. generalized Hooke's law accounting for linear elastic material behavior

$$\boldsymbol{\sigma}(\underline{x}) = \mathbb{C}(\underline{x}) : \boldsymbol{\varepsilon}(\underline{x}), \tag{1}$$

static equilibrium conditions (disregarding volume forces)

$$\mathrm{div}\boldsymbol{\sigma}(\underline{x}) = 0, \tag{2}$$

and linear strain–displacement relations

$$\boldsymbol{\varepsilon}(\underline{x}) = \frac{1}{2}\left(\boldsymbol{\nabla}\underline{\xi} + {}^{t}\boldsymbol{\nabla}\underline{\xi}\right), \tag{3}$$

where $\underline{x}$ denotes the position vector, $\boldsymbol{\sigma}$ and $\boldsymbol{\varepsilon}$, respectively, stand for the second-order tensors of stresses and strains, $\mathbb{C}$ for the fourth-order elastic stiffness tensor, and $\underline{\xi}$ for the displacement vector. The boundaries $\partial\Omega$ of the RVEs are subjected to linear displacements corresponding to a second-order strain tensor $\mathbf{E}$, i.e. we prescribe so-called Hashin boundary conditions [23], also referred to as uniform strain boundary conditions

$$\underline{\xi}(\underline{x}) = \mathbf{E}\cdot\underline{x}. \tag{4}$$

2.3. Homogenization of elasticity

The geometric compatibility of the microscopic strain field $\boldsymbol{\varepsilon}(\underline{x})$ with the uniform strain boundary condition (Eq. (4)) implies the following strain average rule

$$\mathbf{E} = \frac{1}{\Omega}\int_{\Omega}\boldsymbol{\varepsilon}(\underline{x})dV = \sum_{p} f_p\boldsymbol{\varepsilon}_p, \tag{5}$$

where p denotes an index running over all phases of the considered RVE, $f_p = \Omega_p/\Omega$ stands for the volume fraction of phase p, and $\boldsymbol{\varepsilon}_p$ for the second-order tensor of average phase strains defined as

$$\boldsymbol{\varepsilon}_p = \frac{1}{\Omega_p}\int_{\Omega_p}\boldsymbol{\varepsilon}(\underline{x})dV, \tag{6}$$

where Ω_p denotes the subvolume of the RVE occupied by phase p.

Analogously to Eq. (5), macroscopic stresses $\boldsymbol{\Sigma}$ are set equal to the spatial average of the equilibrated local stresses $\boldsymbol{\sigma}(\underline{x})$ inside the RVE,

$$\boldsymbol{\Sigma} = \frac{1}{\Omega}\int_{\Omega}\boldsymbol{\sigma}(\underline{x})dV = \sum_{p} f_p\boldsymbol{\sigma}_p, \tag{7}$$

with $\boldsymbol{\sigma}_p$ as the second-order tensor of average phase stresses, defined by analogy to Eq. (6).

Linearity of the field Eqs. (1)–(3) implies a linear strain concentration rule

$$\boldsymbol{\varepsilon}_p = \mathbb{A}_p : \mathbf{E}, \tag{8}$$

with $\mathbb{A}_p$ as the fourth-order strain concentration tensor of phase p. Specification of the elastic constitutive law of phase p

$$\boldsymbol{\sigma}_p = \mathbb{C}_p : \boldsymbol{\varepsilon}_p, \tag{9}$$

for the strain concentration rule (Eq. (8)) and insertion of the resulting expression for the phase stresses $\boldsymbol{\sigma}_p$ into the stress average rule (Eq. (7)) delivers a relation between macrostress $\boldsymbol{\Sigma}$ and macrostrain $\mathbf{E}$. Comparison of this relation with the macroscopic elastic law $\boldsymbol{\Sigma} = \mathbb{C}^{hom} : \mathbf{E}$ allows for identification of the homogenized elasticity tensor as [17]

$$\mathbb{C}^{hom} = \sum_{p} f_p\mathbb{C}_p : \mathbb{A}_p. \tag{10}$$

Knowledge of phase strain concentration tensors $\mathbb{A}_p$ opens the door to scale transitions, i.e. it allows for computing average phase strains $\boldsymbol{\varepsilon}_p$ from the macroscopically imposed RVE-strain $\mathbf{E}$, see Eq. (8), and it permits homogenization (upscaling) of phase stiffnesses $\mathbb{C}_p$ to the homogenized elasticity tensor of the RVE, $\mathbb{C}^{hom}$, see Eq. (10). As a rule, the concentration tensors $\mathbb{A}_p$ are not known up to analytical precision. Still, they can be estimated based

on classical matrix-inclusion problems of Eshelby [24] and Laws [25], for details see Zaoui [20] and Benveniste [26]

$$\mathbb{A}_p = \left[\mathbb{I} + \mathbb{P}_p^0 : \left(\mathbb{C}_p - \mathbb{C}^0\right)\right]^{-1} : \\ : \left\{\sum_q f_q [\mathbb{I} + \mathbb{P}_q^0 : (\mathbb{C}_q - \mathbb{C}^0)]^{-1}\right\}^{-1}. \tag{11}$$

Specification of Eq. (10) for Eq. (11) delivers the related estimate of the homogenized elastic stiffness tensor as

$$\mathbb{C}^{hom} = \sum_p f_p \mathbb{C}_p : \left[\mathbb{I} + \mathbb{P}_p^0 : \left(\mathbb{C}_p - \mathbb{C}^0\right)\right]^{-1} : \\ : \left\{\sum_q f_q [\mathbb{I} + \mathbb{P}_q^0 : (\mathbb{C}_q - \mathbb{C}^0)]^{-1}\right\}^{-1}. \tag{12}$$

In Eqs. (11) and (12), $\mathbb{P}_p^0$ denotes the fourth-order Hill tensor, accounting for the characteristic shape of phase p embedded in a matrix with stiffness $\mathbb{C}^0$. Choice of $\mathbb{C}^0$ describes the interactions between material phases, see Section 3.2 for details.

2.4. Homogenization of strength

In the line of earlier work on cementitious materials [13,14], on bone biomaterials [27], and on gypsum [28], we here model quasi-brittle fracture in the framework of an elasto-brittle approach. Microscopic phase failure resulting in the failure of the entire RVE is governed by strain peaks rather than by average phase strains defined in Eq. (6). Strain levels corresponding to volumetric and deviatoric strain peaks can be estimated by corresponding quadratic strain averages [29,30]. They can be easily derived from the elastic energy stored in the RVE, provided that the phases within the RVE exhibit isotropic elastic behavior

$$\mathbb{C}_p = 3k_p \mathbb{J} + 2\mu_p \mathbb{K}, \tag{13}$$

where $\mathbb{C}_p$ denotes the fourth-order isotropic elasticity tensor of phase p, k_p and μ_p, respectively, denote the bulk modulus and the shear modulus of phase p, $\mathbb{K}$ stands for the deviatoric part of the fourth-order unity tensor, being defined as $\mathbb{K} = \mathbb{I} - \mathbb{L}$, with $\mathbb{I}$ as the symmetric fourth-order unity tensor with components $I_{ijrs} = 1/2(\delta_{ir}\delta_{js} + \delta_{is}\delta_{jr})$, and $\mathbb{J} = 1/3(\mathbf{1} \otimes \mathbf{1})$ stands for the volumetric part of the fourth-order unity tensor, where $\mathbf{1}$ denotes the second-order unity tensor with components δ_{ij} (Kronecker delta), $\delta_{ij} = 1$ for $i = j$, and $\delta_{ij} = 0$ otherwise. The expression for the quadratic average of the deviatoric strain field over a general phase p reads as [29,30]

$$\overline{\overline{\varepsilon_p^{dev}}} = \sqrt{\frac{1}{\Omega_p}\int_{\Omega_p} \frac{1}{2}\boldsymbol{\varepsilon}^{dev}(\underline{x}) : \boldsymbol{\varepsilon}^{dev}(\underline{x}) dV} \\ = \sqrt{\frac{1}{4f_p}\mathbf{E} : \frac{\partial \mathbb{C}^{hom}}{\partial \mu_p} : \mathbf{E}}, \tag{14}$$

where $\boldsymbol{\varepsilon}^{dev}(\underline{x})$ denotes the field of the deviatoric strain tensor, defined as $\boldsymbol{\varepsilon}^{dev}(\underline{x}) = \boldsymbol{\varepsilon}(\underline{x}) - [\mathrm{tr}\,\boldsymbol{\varepsilon}(\underline{x})/3]\mathbf{1}$. The related quadratic average of the deviatoric stress field is used as an estimate for deviatoric stress peaks and follows simply as

$$\overline{\overline{\sigma_p^{dev}}} = \sqrt{\frac{1}{\Omega_p}\int_{\Omega_p} \frac{1}{2}\mathbf{s}(\underline{x}) : \mathbf{s}(\underline{x}) dV} = 2\mu_p \overline{\overline{e_p^{dev}}} \tag{15}$$

where $\mathbf{s}(\underline{x})$ denotes the field of the deviatoric stress tensor, defined as $\mathbf{s}(\underline{x}) = \boldsymbol{\sigma}(\underline{x}) - [\mathrm{tr}\,\boldsymbol{\sigma}(\underline{x})/3]\mathbf{1}$. Note that Eqs. (14) and (15) refer to non-pressurized fluid phases (water and air), which is in agreement with strength tests performed under atmospheric pressure and under drained conditions (see Section 4).

3. Continuum micromechanics of cement paste and mortar

3.1. Micromechanical representation

For cement paste, we employ two RVEs (Fig. 1): The first one relates to a polycrystalline hydrate foam (with spherical phases representing water and air, and with needle-shaped phases of hydration products exhibiting isotropically distributed orientations, see Fig. 1(a)), and the second one relates to cement paste (with a spherical phase representing clinker embedded in a continuous hydrate foam matrix, see Fig. 1(b)). As for mortar, we adopt the micromechanical representation of Bernard et al. [31]: An RVE of mortar comprises a spherical phase representing sand grains embedded in a continuous cement paste matrix, see Fig. 1(c).

3.2. Upscaling of elasticity

Homogenization step I refers to the hydrate foam. Since the hydration products are mutually interacting, as in a polycrystal, use of the self-consistent scheme [32–35] is appropriate for determining the homogenized stiffness tensor of the hydrate foam: $\mathbb{C}_{hf}^{hom}$. Accordingly, $\mathbb{C}^0$ in Eq. (12) is chosen to be equal to the homogenized stiffness of the hydrate foam itself, and the sum over p in Eq. (12) now extends over the air and water phases, as well as over an infinite amount of hydrate phases oriented in all space directions indicated by polar angles φ and ϑ. Consequently, we arrive at the following implicit tensorial expression for $\mathbb{C}_{hf}^{hom}$:

$$\mathbb{C}_{hf}^{hom} = \left\{\sum_p \tilde{f}_p \mathbb{C}_p : [\mathbb{I} + \mathbb{P}_{sph}^{hf} : (\mathbb{C}_p - \mathbb{C}_{hf}^{hom})]^{-1} + \tilde{f}_{hyd}\mathbb{C}_{hyd} : \right. \\ \left. \int_0^{2\pi}\int_0^{\pi} \left[\mathbb{I} + \mathbb{P}_{cyl}^{hf}(\varphi,\vartheta) : (\mathbb{C}_{hyd} - \mathbb{C}_{hf}^{hom})\right]^{-1} \frac{\sin\vartheta d\vartheta d\varphi}{4\pi}\right\} : \\ \left\{\sum_p \tilde{f}_p [\mathbb{I} + \mathbb{P}_{sph}^{hf} : (\mathbb{C}_p - \mathbb{C}_{hf}^{hom})]^{-1} \right. \\ \left. + \tilde{f}_{hyd}\int_0^{2\pi}\int_0^{\pi} \left[\mathbb{I} + \mathbb{P}_{cyl}^{hf}(\varphi,\vartheta) : (\mathbb{C}_{hyd} - \mathbb{C}_{hf}^{hom})\right]^{-1} \frac{\sin\vartheta d\vartheta d\varphi}{4\pi}\right\}^{-1}. \tag{16}$$

In Eq. (16), $\tilde{f}_{hyd}$, $\tilde{f}_{H_2O}$, and $\tilde{f}_{air}$, respectively, stand for the hydrate foam-related volume fractions of hydration products, water, and air, which depend on the composition and on the maturity of the material, see Section 3.4. For detailed explanations regarding the numerical evaluation of Eq. (16), as well as for computation of the Hill tensors for spherical material phases, $\mathbb{P}_{sph}^{hf}$, and for cylindrical phases, $\mathbb{P}_{cyl}^{hf}$, respectively, see [13,14].

Homogenization step II refers to cement paste. Since the spherical clinker phase is embedded in a continuous matrix built up by the hydrate foam, use of the Mori–Tanaka scheme [20,26,36] is appropriate for determining the homogenized stiffness tensor of cement paste: $\mathbb{C}_{cp}^{hom}$. Accordingly, $\mathbb{C}^0$ in Eq. (12) is chosen to be equal to the homogenized stiffness of the hydrate foam, resulting in the following explicit expression for $\mathbb{C}_{cp}^{hom}$:

$$\mathbb{C}_{cp}^{hom} = \left\{(1-f_{clin})\mathbb{C}_{hf}^{hom} + f_{clin}\mathbb{C}_{clin} : [\mathbb{I} + \mathbb{P}_{sph}^{hf} : (\mathbb{C}_{clin} - \mathbb{C}_{hf}^{hom})]^{-1}\right\} : \\ \left\{(1-f_{clin})\mathbb{I} + f_{clin}[\mathbb{I} + \mathbb{P}_{sph}^{hf} : (\mathbb{C}_{clin} - \mathbb{C}_{hf}^{hom})]^{-1}\right\}^{-1}. \tag{17}$$

In Eq. (17), f_{clin} and $(1 - f_{clin}) = f_{hf}$, respectively, stand for the cement paste-related volume fractions of clinker and of the hydrate foam,

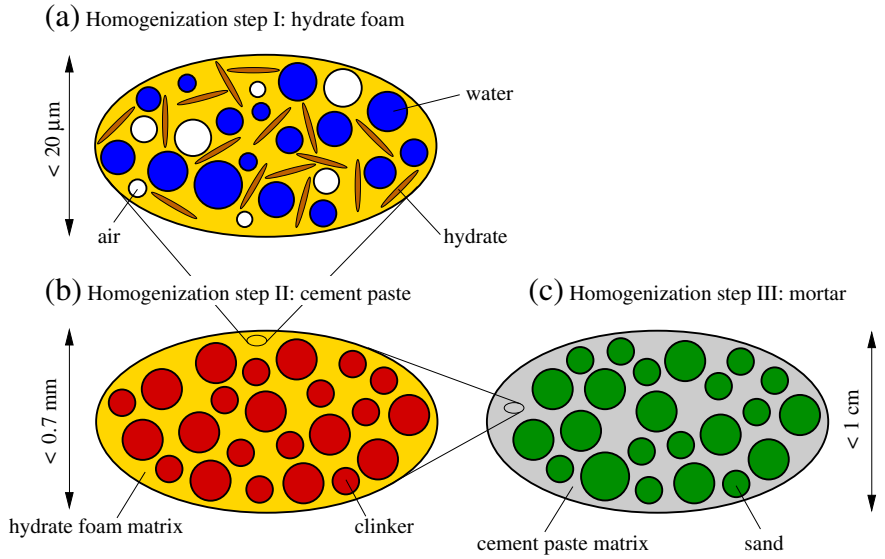

Fig. 1. Micromechanical representation of cement paste and mortar through a two-step and a three-step homogenization scheme, respectively: (a) polycrystalline RVE of "hydrate foam" built up of spherical water and air phases, as well as of needle-shaped hydrate phases oriented uniformly in all space directions (modeled by self-consistent scheme); (b) RVE of matrix-inclusion composite "cement paste" where a spherical clinker phase is embedded in a hydrate foam matrix (modeled by Mori–Tanaka scheme); (c) RVE of matrix-inclusion composite "mortar" where a spherical sand phase is embedded in a cement paste matrix (modeled by Mori–Tanaka scheme); all schematic 2D sketches refer to 3D volume elements.

which depend on the composition and on the maturity of the material, see Section 3.4.

Homogenization step III refers to mortar. Since the spherical sand phase is embedded in a continuous matrix built up by cement paste, use of the Mori–Tanaka scheme is again appropriate for determining the homogenized stiffness tensor of mortar, $\mathbb{C}_{mo}^{hom}$. Accordingly, $\mathbb{C}^0$ in Eq. (12) is chosen to be equal to the homogenized stiffness of cement paste, resulting in the following explicit expression for $\mathbb{C}_{mo}^{hom}$:

$$\mathbb{C}_{mo}^{hom} = \left\{(1-\bar{f}_{san})\mathbb{C}_{cp}^{hom} + \bar{f}_{san}\mathbb{C}_{san} : [\mathbb{I} + \mathbb{P}_{sph}^{cp} : (\mathbb{C}_{san}-\mathbb{C}_{cp}^{hom})]^{-1}\right\} : \left\{(1-\bar{f}_{san})\mathbb{I} + \bar{f}_{san}[\mathbb{I} + \mathbb{P}_{sph}^{cp} : (\mathbb{C}_{san}-\mathbb{C}_{cp}^{hom})]^{-1}\right\}^{-1}. \quad (18)$$

In Eq. (18), $\bar{f}_{san}$ and $(1-\bar{f}_{san}) = \bar{f}_{cp}$, respectively, stand for the mortar-related volume fractions of sand and of the cement paste matrix, which depend on the composition of the material, see Section 3.4.

3.3. Upscaling of strength

According to the elasto-brittle approach of Section 2.4, linear elastic behavior prevails as long as the quadratic deviatoric stress averages over each of the hydrate phases (oriented in all space directions φ and ϑ) remain below a critical strength value $\sigma_{hyd,crit}^{dev}$

$$\max_{\varphi,\vartheta} \overline{\overline{\sigma_{hyd,\varphi,\vartheta}^{dev}}} \leq \sigma_{hyd,crit}^{dev}. \quad (19)$$

The quadratic stress averages depend on the macroscopic strains $\mathbf{E}_{cp}$ imposed onto an RVE of cement paste, as follows from specification of Eqs. (14) and (15) for the hydrate phases of Fig. 1(a), according to

$$\overline{\overline{\sigma_{hyd,\varphi,\vartheta}^{dev}}} = \sqrt{\frac{\mu_{hyd}^2}{\bar{f}_{hyd,\varphi,\vartheta}}\mathbf{E}_{cp} : \frac{\partial \mathbb{C}_{cp}^{hom}}{\partial \mu_{\varphi,\vartheta}} : \mathbf{E}_{cp}}, \quad (20)$$

where the cement paste-related volume fractions $f_{hyd,\varphi,\vartheta}$ of (φ,ϑ)-oriented hydrates are defined as limit cases, for respective computational details, see [13]. The macrostrain $\mathbf{E}_{cp}$ in Eq. (20) is related to the macrostress $\mathbf{\Sigma}_{cp}$ through the inverse elasticity law according to

$$\mathbf{E}_{cp} = \left[\mathbb{C}_{cp}^{hom}\right]^{-1} : \mathbf{\Sigma}_{cp}, \quad (21)$$

with $\mathbb{C}_{cp}^{hom}$ following from Eq. (17).

By analogy, quadratic stress averages in needle-shaped hydrates oriented in (φ,ϑ) direction, which are embedded in an RVE of mortar, follow from deriving the homogenized stiffness of mortar (Eq. (18)) with respect to the shear modulus of those hydrates:

$$\overline{\overline{\sigma_{hyd,\varphi,\vartheta}^{dev}}} = \sqrt{\frac{\mu_{hyd}^2}{\bar{f}_{hyd,\varphi,\vartheta}}\mathbf{E}_{mo} : \frac{\partial \mathbb{C}_{mo}^{hom}}{\partial \mu_{\varphi,\vartheta}} : \mathbf{E}_{mo}}, \quad (22)$$

where $\bar{f}_{hyd,\varphi,\vartheta}$ are the volume fractions of (φ,ϑ)-oriented hydrate phases in an RVE of mortar. $\mathbf{E}_{mo}$ denotes the uniform macrostrain imposed on the RVE of mortar, being itself related to the macrostress $\mathbf{\Sigma}_{mo}$ through the inverse elasticity law

$$\mathbf{E}_{mo} = \left[\mathbb{C}_{mo}^{hom}\right]^{-1} : \mathbf{\Sigma}_{mo}, \quad (23)$$

with $\mathbb{C}_{mo}^{hom}$ following from Eq. (18). It is noteworthy that Eq. (22), together with Eq. (23), can be seen as higher-order concentration relation from the mortar to the hydrate scale. Thereby, we do not "successively" concentrate from one RVE to another, but $\partial \mathbb{C}_{mo}^{hom}/\partial \mu_{\varphi,\vartheta}$ directly entails all information down to the hydrate scale.

Eq. (19), together with Eqs. (20) and (21), as well as with Eqs. (22) and (23), respectively, constitutes a micromechanics-based quasi-brittle failure criterion for cement pastes and for mortars, respectively, considering through derivation of the homogenized stiffness tensors (17) and (18), respectively, the effect of the elastic properties of the elementary constituents of cement pastes and mortars, as well as of their microstructures and compositions. In words, this criterion reads as follows: If, due to (compressive uniaxial) macroscopic load increase, the deviatoric hydrate strength $\sigma_{hyd,crit}^{dev}$ is reached in the most heavily stressed region of the hydrate phases, the elastic limit on the microscale is reached, which, in turn, corresponds to the ultimate

load bearable by the RVE (of cement paste and of mortar, respectively). An algorithm for evaluation of Eq. (20), i.e. for computation of deviatoric stress peaks in needle-shaped hydrates within a two-step homogenization approach, is presented in [14]. For the computations reported herein, it was straightforwardly extended in order to deal with the three-step homogenization approach described for mortar.

3.4. Model input values: volume fractions and elasticity properties of material phases

The evolution of cement paste-related phase volume fractions during hydration is accounted for by the Powers–Acker hydration model [37,38], providing cement paste-related volume fractions of clinker, water, hydration products, and air:

$$\begin{aligned} f_{clin}(\xi) &= \frac{1-\xi}{1+\frac{\rho_{clin}}{\rho_{H_2O}}(w/c)} = \frac{20(1-\xi)}{20+63(w/c)} \geq 0, \\ f_{H_2O}(\xi) &= \frac{\rho_{clin}[(w/c)-0.42\xi]}{\rho_{H_2O}\left[1+\frac{\rho_{clin}}{\rho_{H_2O}}(w/c)\right]} = \frac{63[(w/c)-0.42\xi]}{20+63(w/c)} \geq 0, \\ f_{hyd}(\xi) &= \frac{1.42\rho_{clin}\xi}{\rho_{hyd}\left[1+\frac{\rho_{clin}}{\rho_{H_2O}}(w/c)\right]} = \frac{43.15\xi}{20+63(w/c)}, \\ f_{air}(\xi) &= 1-f_{clin}-f_{H_2O}-f_{hyd} = \frac{3.31\xi}{20+63(w/c)}. \end{aligned} \tag{24}$$

In Eq. (24), $\rho_{clin}=3.15$ kg/dm^3 [39], $\rho_{H_2O}=1$ kg/dm^3, and $\rho_{hyd}=2.073$ kg/dm^3 [40] are the mass densities of clinker, water, and hydrates, respectively; w/c denotes the water-to-cement mass ratio, and ξ stands for the hydration degree which is defined as the mass of currently formed hydrates over the mass of hydrates formed at completed hydration. Air-filled pores are created since hydration products occupy a smaller volume than the reactants clinker and water.

Hydrate foam-related volume fractions of hydration products, water, and air ($\tilde{f}_{hyd}, \tilde{f}_{H_2O}$, and $\tilde{f}_{air}$), as occurring in Eq. (16), follow from the cement paste-related volume fractions of clinker, water, hydration products, and air ($f_{clin}, f_{H_2O}, f_{hyd}$, and f_{air}, given in Eq. (24)), according to

$$\tilde{f}_j = \frac{f_j}{1-f_{clin}} \qquad j = \begin{cases} hyd, \\ H_2O, \\ air. \end{cases} \tag{25}$$

The mortar-related phase volume fractions of cement paste and sand, occurring in Eq. (18), depend on both the water-to-cement mass ratio w/c and the sand-to-cement mass ratio s/c

$$\bar{f}_{san} = \frac{\frac{s/c}{\rho_{san}}}{\frac{1}{\rho_{clin}}+\frac{w/c}{\rho_{H_2O}}+\frac{s/c}{\rho_{san}}} \qquad \bar{f}_{cp} = 1-\bar{f}_{san} \tag{26}$$

with the mass density of quartz amounting to $\rho_{san}=2.648$ kg/dm^3 [41].

Elasticity constants listed in Table 1 comprise mixture-independent ("universal") values for clinker, water, air, and quartz taken from the open literature, while, for the sake of simplicity, the properties of "hydration products" are averages over all types of hydrates, including Portlandite, Ettringite, and Calcium Silicate Hydrates (C–S–H) of different mass densities.

As to get direct access to such "average" elasticity constants of hydrates, it would be desirable to produce a material sample consisting of hydration products only, and to perform elasticity tests on such a material. Deplorably, this is not possible. As a remedy, we consider the material coming closest to the aforementioned "pure hydrate", i.e. to the situation where, in Fig. 1, the volume fractions of water, air, and clinker are close to zero, while the volume fraction of hydrates approaches one. According to the Powers–Acker hydration model, the aforementioned volume fractions are most closely attained in a fully-hydrated ($\xi=1$) cement paste with water–cement ratio amounting to 0.42. These volume fractions are:

$$f_{clin}=f_{H_2O}=0, \quad f_{hyd}=92.9\%, \quad f_{air}=7.1\%. \tag{27}$$

To get experimental access to the elastic properties of such a "close-to-a-pure-hydrate" cement paste, we consider data of Helmuth and Turk [42]. These authors tested three different types of cement pastes: one was produced on the basis of almost pure tricalcium silicate (C_3S), while the remaining two were based on (two, different) Portland cements. Water–cement ratios ranged from 0.3 to 0.6. Young's modulus was deduced from measurements of the fundamental flexural and torsional resonance frequencies of specimens that were allowed to cure for six to 14 months (C_3S samples) and for six to 24 months (Portland cement samples), respectively, see Fig. 2. Given these long-lasting curing times, the corresponding values for Young's modulus are commonly assigned to *fully hydrated* cement pastes [43]. While, in [42], such experimental values are not documented for $w/c=0.42$, the numerous data related to w/c values around 0.42 allow for an interpolation which yields the Young's modulus of fully hydrated cement paste with $w/c=0.42$ (i.e. that of almost pure hydrates) as 25 GPa, see circle in Fig. 2.

In the following, we will use the elasticity model of Section 3.2 to identify from the Young's modulus of almost pure hydrates (hydrates foams with 7.1% capillary porosity, see Eq. (27)) that of pure hydrates (without capillary porosity). Volume fractions of the almost pure hydrate foam follow from specification of Eq. (27) for $\xi=1$ and $w/c=0.42$ as

$$\tilde{f}_{H_2O}=0, \quad \tilde{f}_{hyd}=92.9\%, \quad \tilde{f}_{air}=7.1\%. \tag{28}$$

(i) Specifying the elasticity model (17) for Eqs. (28), for vanishing bulk and shear moduli of air (see Table 1), as well as for the Poisson's ratio of Calcium–Silicate–Hydrates (C–S–H) [31], which is taken as the characteristic average for all hydrates: $\nu_{CSH}=\nu_{hyd}=0.24$, and (ii) setting up the condition that the model-predicted Young's modulus of the hydrate foam is to be equal to 25 GPa, i.e. $E_{hf}^{hom}(\xi=1, w/c=0.42)=25$ GPa,[1] allows for iterative determination of the sought value for the average Young's modulus of hydrates as $E_{hyd}=29.158$ GPa. Corresponding average bulk and shear moduli for the hydration products are given in Table 1.

A first relevance check of these hydrate moduli can be made when predicting the experimental data of Fig. 2, referring to cement pastes with a wide range of water–cement ratios: Therefore, the two-step homogenization scheme (Eqs. (16) and (17)) needs to be specified for the identified average hydrate elasticity constants, for the mixture-independent ("universal") elastic properties of clinker, for the

Table 1
Mixture-independent ("universal") elastic properties of clinker, water, hydration products, air, and quartz.

Phase	Bulk modulus	Shear modulus	Source
	k [GPa]	μ [GPa]	
Clinker	$k_{clin}=116.7$	$\mu_{clin}=53.8$	[38]
Water	$k_{H_2O}=0.0$	$\mu_{H_2O}=0.0$	[31]
Hydration products	$k_{hyd}=18.7$	$\mu_{hyd}=11.8$	[31,42], see text
Air	$k_{air}=0.0$	$\mu_{air}=0.0$	
Quartz (sand)	$k_{san}=37.8$	$\mu_{san}=44.3$	[41]

[1] The relation between Young's modulus E_{hf}^{hom} and tensor components C_{1212}^{hom} and C_{1111}^{hom} of the homogenized stiffness tensor $\mathbb{C}_{hf}^{hom}$ reads as $E_{hf}^{hom}=\frac{C_{1212}^{hom}\left(3C_{1111}^{hom}-4C_{1212}^{hom}\right)}{C_{1111}^{hom}-C_{1212}^{hom}}$.

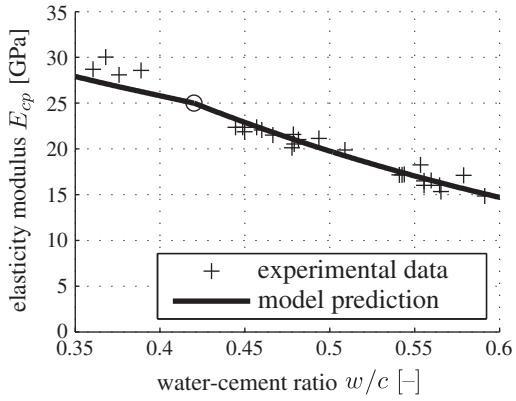

Fig. 2. Final Young's modulus of cement paste: experimental results by Helmuth and Turk [42], taken from [43], and predictions according to Eqs. (19), (20), (21), (17), (16), (24), and (25), specified for mechanical properties from Table 1.

vanishing effective stiffnesses of the drained fluid phases "air" and "water", see Table 1, as well as for the phase volume fractions (24) and (25) specified for the maximum attainable hydration degree

$$\max \xi = \begin{cases} \frac{w/c}{0.42} & \text{for} \quad w/c \le 0.42 \\ 1 & \text{for} \quad w/c \ge 0.42 \end{cases}. \tag{29}$$

Model predictions and experiments agree very well (Fig. 2). Notably, the functional relationship between final Young's modulus and water–cement ratio exhibits a kink at $w/c = 0.42$, because in substoichiometric cement pastes ($w/c < 0.42$) the available water does not suffice for hydration of the entire clinker—the chemical reaction stops at a hydration degree smaller than one, see Eq. (29).

3.5. Performance of elasticity and strength models

Herein, we provide model-predicted evolutions of elasticity and strength of hydrating cement pastes with water–cement ratios ranging from 0.157 to 0.8. As expected, the hydration degree-induced stiffness increase is larger the lower the water–cement ratio (Fig. 3(a) and (b)), and interestingly, this increase is of convex nature for high water–cement ratios, but of S-shaped nature for smaller water–cement ratios, for both bulk and shear modulus evolutions (see Fig. 3 (a) and (b)). In all model predictions, non-zero stiffnesses are reached already for very early hydration degrees, and this is due to the prolate ("infinitely long") hydrate shape adopted herein. It might be more realistic to introduce "cigars" with an aspect ratio somewhat smaller than infinity, if precise percolation modeling would be the key feature of interest. Herein, however, our focus is on strength, see Fig. 4 for the model-predicted uniaxial compressive strength of cement paste, normalized by the deviatoric hydrate strength. In contrast to the elastic predictions, strength turns out to be an always convex function of the hydration degree, whose slope obviously increases with decreasing water–cement ratio.

4. Validation of strength models for cement paste and mortar

4.1. Strength validation on cement paste level

Aiming at a strictly quantitative test of the predictive capabilities of the presented strength model for cement paste, we now compare model predictions with independent experimental data. Taplin [15] used a normal Portland cement to produce cement pastes with water–cement ratios ranging from 0.157 to 0.8. All samples were right rectangular prisms measuring $4 \times 0.5 \times 0.5$ in. They were cured at 25 °C. At the time of testing, the prisms were broken into two halves

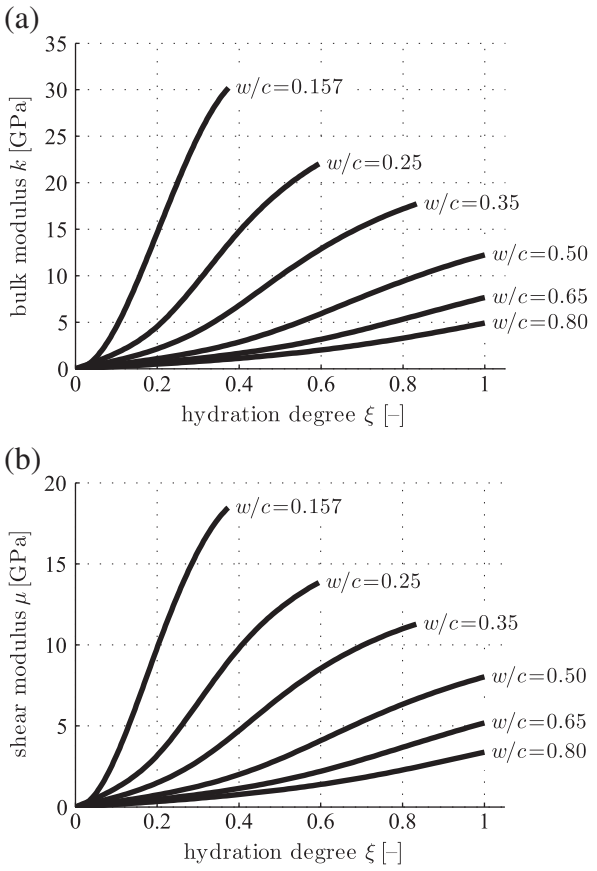

Fig. 3. Model-predicted elasticity evolutions of cement pastes (a) bulk modulus and (b) shear modulus.

resulting in two specimens measuring $2 \times 0.5 \times 0.5$ in. Each specimen was tested in uniaxial compression by placing it on one of its sides on the platform of a small hydraulic press and forcing it against a 0.373 in. wide steel spacer which lay perpendicular to the bars. Two destructive tests could be carried out on each specimen, because an effective specimen length of less than three-quarters of an inch was destroyed in each of the compression tests. Because the crushed part did not always correspond exactly to the area of the load plate, Taplin [15] directly published the actually measured ultimate forces, rather than postprocessing them into compressive strength values, see the ordinate in Fig. 5. After testing, Taplin [15] determined the bound water content of the crushed samples, H/C, see abscissa in Fig. 5.

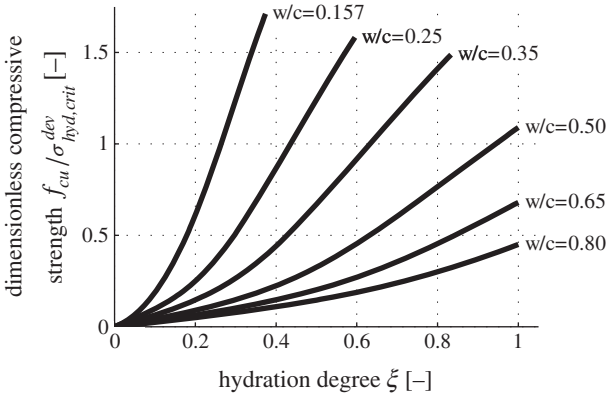

Fig. 4. Model-predicted dimensionless compressive strength evolution of hydrating cement pastes.

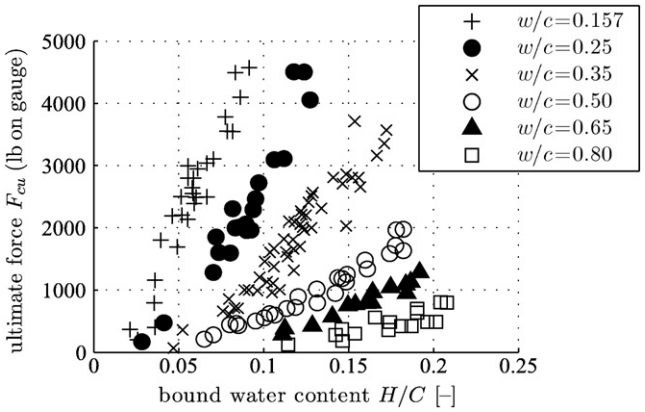

Fig. 5. Ultimate force values measured in similar uniaxial compression tests on hydrating cement pastes: experimental results of Taplin [15].

In order to make our model predictions comparable to the experimental results of Taplin [15], we have to establish relations between the coordinates of Figs. 4 and 5, which should be preferably independent of the unknown value of $\sigma^{dev}_{hyd,crit}$. As for the abscissae of Figs. 4 and 5, we recall the stoichiometric relationship between the bound water content H/C and the hydration degree ξ, which standardly reads for the average hydrates considered herein as [44]

$$H/C = 0.25\xi. \tag{30}$$

In order to transform the ordinates of Figs. 4 and 5 into comparable dimensionless ordinates (i) we divide the ordinate values of Fig. 4 by the dimensionless compressive strength predicted for a fully-hydrated cement paste with $w/c = 0.157$, i.e. by $\max[f_{cu}/\sigma^{dev}_{hyd,crit}] = f_{cu}(w/c = 0.157, \xi = 0.374)/\sigma^{dev}_{hyd,crit} = 1.7117$, and (ii) we divide the ordinate values of Fig. 5 by the maximum ultimate force measured on samples with $w/c = 0.157$, i.e. by $\max F_{cu} = 4573.2$lb, see Fig. 6 for the obtained result. This normalization makes sense since Taplin [15] measured the largest ultimate force on a sample of $w/c = 0.157$, which exhibited $\xi = 0.366$; and this is only 2% smaller than the largest hydration degree possible at this w/c-value, amounting to $\max\xi = 0.157/0.42 = 0.374$, see Eq. (29).

Model-predicted strength evolutions agree satisfactory with corresponding independent results of Taplin [15], see Fig. 6. Quantitatively speaking, the quadratic correlation coefficient is as high as $r^2 = 93\%$, while the mean prediction error and the standard deviation amount to -3% and to 7.3%, respectively. This is even more remarkable when recalling that the model predictions illustrated in Fig. 6 do not depend on the unknown deviatoric strength of the hydration products, but only on the elasticity model proposed herein, i.e. the elasticity constants listed in Table 1, on the Powers–Acker hydration model-related volume fractions (24) and (25), as well as on the morphological representation of cement paste, including the hierarchical organization, the mode of phase interactions, and the phase shapes illustrated in Fig. 1. Given the simplicity of the proposed model and the vast range of considered water–cement ratios, we regard the model to be validated successfully.

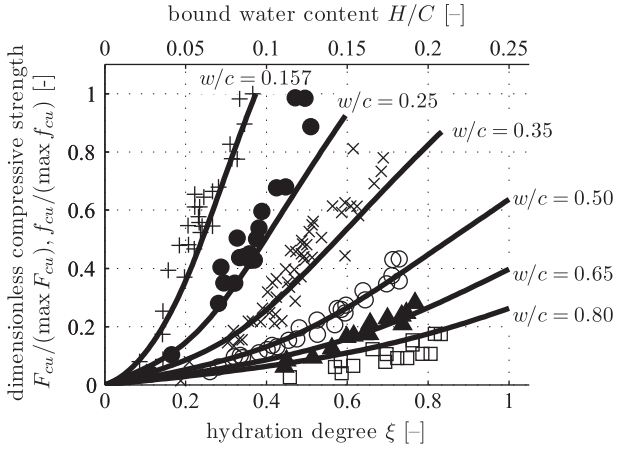

Fig. 6. Strength evolution of hydrating cement pastes: experimental results of Taplin [15] and predictions of the proposed model.

4.2. Strength validation on mortar level

European standard EN 196-1 [16] identifies "strength of cement" (the strength of stoichiometric cement paste, $w/c = 0.42$) with the mean 28 day uniaxial compressive strength of prismatic *mortar* specimens with water-to-cement and sand-to-cement mass ratios of $w/c = 0.5$ and $s/c = 3.0$, respectively. This standard mortar has to be produced with CEN reference sand, a natural quartz sand with rounded grains exhibiting an SiO_2 mass fraction of at least 98%.

We now investigate whether the presented elasto-brittle strength model is able to predict the aforementioned, very notable, identity of mortar and cement strengths. As regards strength model predictions for mortar, we specify the strength criterion (Eq. (19)) for quadratic stress averages in hydrates embedded in an RVE of mortar, see Eq. (22). The elasticity constants of quartz required for evaluation of the involved stiffness estimate C^{hom}_{mo} according to (18), are taken from a standard handbook of physical constants [41], see Table 1.

Model-predicted strength evolutions for cement pastes and mortars significantly depend on the water–cement ratio, notably also in the range $w/c = 0.42 \ldots 0.50$, the limits of which are related to stoichiometric cement paste and standard mortar, respectively (Fig. 7). Nevertheless, the model-predicted strength of standard mortar ($w/c = 0.50$ and $s/c = 3.0$) is, on average, by as little as -0.54% smaller than the model-predicted strength of stoichiometric cement paste ($w/c = 0.42$), see Fig. 8. Besides, it is remarkable that the identity of Fig. 8 holds for any degree of hydration, not just for the one attainable after 28 days. This virtual identity of model results is a further, strong indication for the validity of our elasto-brittle strength approach.

5. General model characteristics—uniaxial cement paste strength as a function of water–cement ratio and of hydration degree

Complementing model predictions shown in Fig. 4, we here provide further dimensionless insight into characteristics of the elasto-brittle strength model for cement paste:

- Uniaxial compressive strength values of *different* cement pastes, exhibiting the *same* hydration degree, increase overlinearly with decreasing water–cement ratio, see Fig. 9.
- Final strength values of (fully-hydrated) cement pastes increase monotonically with decreasing water–cement ratio, see Fig. 9. Notably, this functional relationship exhibits a kink at $w/c = 0.42$, because in substoichiometric cement pastes ($w/c < 0.42$) the available water does not suffice for hydration of the entire clinker —the chemical reaction stops at a hydration degree smaller than one, see Eq. (29) and Fig. 9.
- Hydration degrees required to reach a specific strength of cement paste increase almost linearly with increasing water–cement ratio, see Fig. 10.

6. Discussion

We here relate overall stresses acting on cement pastes and mortars to higher-order deviatoric stress averages in needle-shaped hydrates. When the latter stresses reach a critical strength value, the

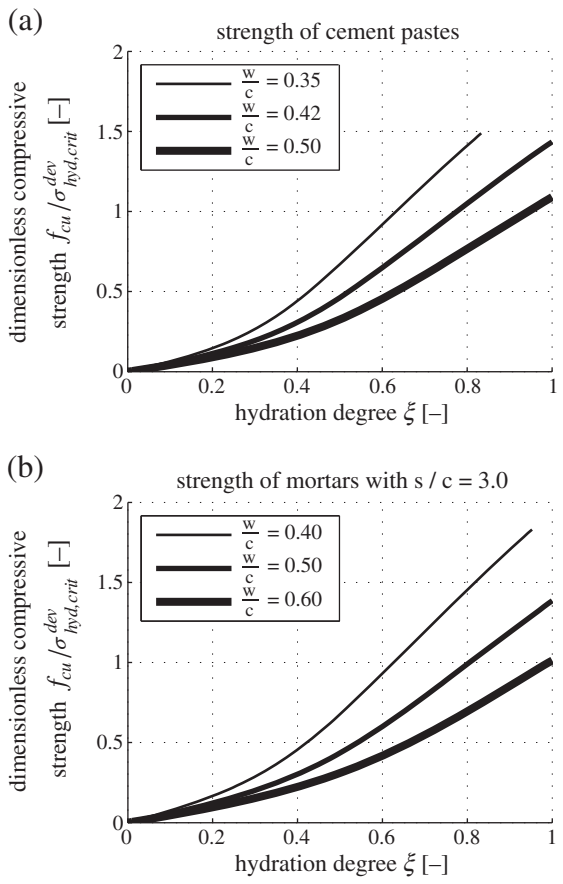

Fig. 7. Model-predicted strength evolutions (a) of cement pastes, and (b) of mortars with sand-to-cement mass ratios $s/c = 3.0$.

overall stresses refer to the (quasi-brittle) macroscopic uniaxial compressive strength of cementitious materials. In this context, a single deviatoric hydrate strength can explain, via higher-order average upscaling within a two-step random homogenization scheme, the uniaxial compressive strengths of cement pastes, as functions of the hydration degree, over a wide range of water–cement ratios (see Fig. 6). Since the experimental data were all normalized to a maximum strength attained by a material with a very low water–cement ratio, our upscaling scheme did not even require a numerical value for the deviatoric hydrate strength to be introduced—this may be regarded as an additional indication for the validity of our approach, as was the model prediction of the equivalence of strength

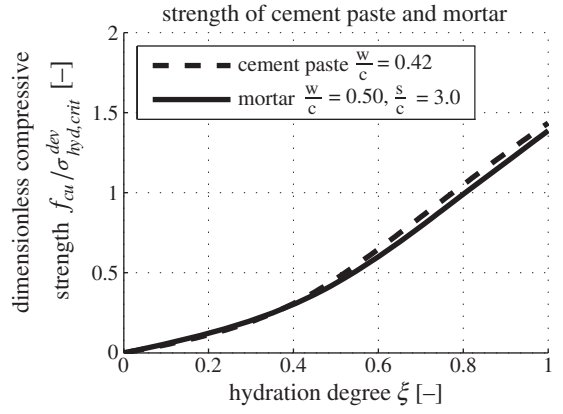

Fig. 8. Comparison of model-predicted strength evolutions of stoichiometric cement paste ($w/c = 0.42$) and of standard mortar [16] with $w/c = 0.5$ and $s/c = 3.0$.

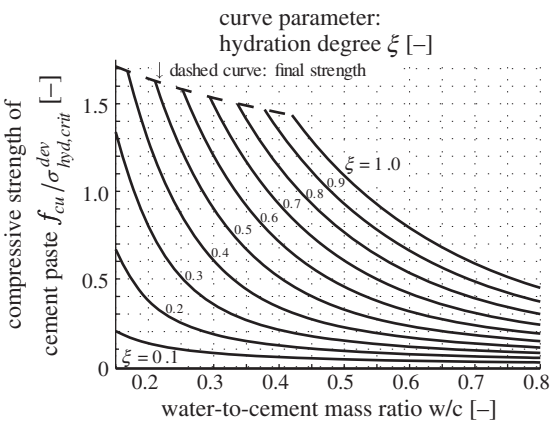

Fig. 9. Model-predicted evolutions of uniaxial compressive strength of cement paste (normalized by deviatoric hydrate strength) as a function of water-to-cement mass ratio w/c and of hydration degree ξ.

of stoichiometric cement paste to that of EN 196-1 standard mortar, modeled as a three-scale material.

We re-iterate from our earlier contributions [13,14] that the needle-type shape of the hydrates is an essential feature for the success of the present micromechanics formulation. Choice of this phase shape is consistent with observations of Richardson [10]: According to Fig. 6 of [10], outer products typically have the shape of needles which are about 100 nm wide and a few micrometers long. Thus, as concerns the outer products, there is just one order of magnitude between the size of the material phases and that of the RVE of the hydrate foam in Fig. 1(a). On the other hand, the needles forming the inner products are smaller, namely several nanometers thick and some tens of nanometers long, as is seen in Fig. 8 of [10] as well as in Figs. 4 and 5 of [11]. Such differences in the size of phases in one and the same homogenization step are, however, quite usual in applied micromechanics of materials: E.g., our homogenization step II, which is somewhat similar to that proposed by Constantinides and Ulm [40], also comprises clinker grains spanning typically two orders of magnitude in size.

For the sake of simplicity, we here do not distinguish between different types of hydrates (such as low density calcium–silicate–hydrates (LD C–S–H) and high density calcium–silicate–hydrates (HD C–S–H)), but identify, from dense hydrate foams with very low capillary porosity, elastic properties which are, on average, representative for all hydration products. Such "average" hydrate phase

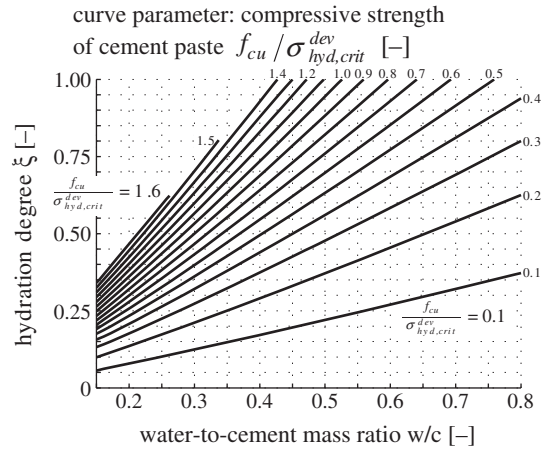

Fig. 10. Model-predicted evolutions of uniaxial compressive strength of cement paste (normalized by deviatoric hydrate strength) as a function of hydration degree ξ and of water-to-cement mass ratio w/c.

properties have been repeatedly used in concrete micromechanics [45,46].

If one wishes to elaborate the model towards consideration of several hydraulic phases (including di- and tricalcium silicate, tricalcium aluminate, and calcium aluminoferrite) and/or of several hydration product families (including calcium–silicate–hydrates of all densities, calcium hydroxide crystals "portlandite", and hexacalcium aluminate trisulfate hydrates "ettringite"), such as reported in e.g. [31,43,47,48], the clinker phase and/or the hydration product phases could be further subdivided. Thereby, it would be necessary to consider the dependence of the hydrate subphase concentrations on water–cement ratio, hydration degree, and heat treatment [49,50].

When absolute, rather than normalized, strength values are of interest, we need to introduce a number for the deviatoric hydrate strength, which can be identified from classical macroscopic tests on cement pastes. Setting, for instance, the uniaxial compressive strength $f_{cu}=54.1$ MPa of a cement paste with a water–cement ratio amounting to 0.50 [51] equal to corresponding model predictions for a fully-hydrated paste from Fig. 4, suggests a value for the deviatoric hydrate strength of

$$\sigma^{dev}_{hyd,crit} \approx 50\,\text{MPa}. \tag{31}$$

When inscribing a Tresca failure surface into the cylindrical von Mises surface defined by Eq. (31), we arrive at an estimate for the hydrate cohesion (pure shear strength), namely

$$c_{hyd} = \sigma^{dev}_{hyd,crit}\frac{\sqrt{3}}{2} \approx 43.3\,\text{MPa}. \tag{32}$$

It is interesting to discuss this value in view of yield design approaches for nanoindentation with a Berkovich tip [52]: In this context, the hydrate cohesion (Eq. (32)) relates to an interval of hardness values, namely to $H_{hyd}\in[271.5,1704]$ MPa when considering friction angles between 3 and 30° according to Fig. 6 of [52]. Indeed, corresponding nanoindentation measurements for low density C–S–H and for high density C–S–H, amounting to $H_{LD}=450$ MPa and to $H_{HD}=830$ MPa, respectively, see [53], lie well within the aforementioned interval.

Finally, we remark current limitations of our approach: it focuses on the micro-to-macro transition, thereby leaving aside open challenges in the micro-to-nano transition: Low and high density C–S–H are agglomerates consisting of elementary bricks with gel porosity in between. Recent molecular dynamics simulations [54] suggest the pure shear strength of a 1.4 nm-sized elementary block of C–S–H to be as high as 1 GPa. One could speculate that the far lower strength values at the level of low-density and high-density C–S–H (in the order of 50 MPa according to Eqs. (31) and (32)) result from weak interfaces between the elementary blocks, as well as from the gel porosity. As a second limitation of the current work, the validation examples in the present work do not comprise multiaxial stress states, and the latter might well require extension or modification of the proposed hydrate strength criterion (Eq. (19)), probably in the direction of a Mohr–Coulomb or Drucker–Prager criterion. For elucidation of such issues, biaxial strength experiments could be the basis for the next attempt to "falsify", in the sense of Popper [55], our approach. Also, when it comes to strength design of large structures, size-effect scaling may become relevant [56].

Thirdly, the applicability of our model is limited to non-pressurized (drained) pores, in consistency with the test results considered herein. When it comes to quantification of strength properties under undrained conditions or during drying where surface tensions become significant, extension of the model towards microporomechanics [30,57–59] appears as a natural option for future activities.

Acknowledgment

The authors are grateful to the anonymous reviewers whose constructive and comprehensive comments have helped us to significantly improve our manuscript, particularly with respect to the explanation of the micromechanical concept and to a deeper discussion on the potentials and limitations of the presented approach.

References

[1] S. Chatterji, J.W. Jeffery, Three-dimensional arrangement of hydration products in set cement paste, Nature 209 (5029) (1966) 1233–1234.
[2] W. Richartz, Development of texture and strength in hardened cement paste, Beton 19 (5) (1969) 203–206, In German.
[3] T.D. Ciach, J.E. Gillott, E.G. Swenson, P.J. Sereda, Microstructure of hydrated portland cement pastes, Nature 227 (5262) (1970) 1045–1046.
[4] S. Chatterji, J.W. Jeffery, Further studies of the three-dimensional arrangement of the hydration products of portland cements, Indian Concrete Journal 45 (4) (1971) 167–172.
[5] T.D. Ciach, J.E. Gillott, E.G. Swenson, P.J. Sereda, Microstructure of calcium silicate hydrates, Cement and Concrete Research 1 (1) (1971) 13–25.
[6] R.B. Williamson, Solidification of portland cement, Progress in Materials Science 15 (3) (1972) 189–286.
[7] X.F. Gao, Y. Lo, C.M. Tam, C.Y. Chung, Analysis of the infrared spectrum and microstructure of hardened cement paste, Cement and Concrete Research 29 (6) (1999) 805–812.
[8] J. Tritthart, F. Häußler, Pore solution analysis of cement pastes and nanostructural investigations of hydrated C_3S, Cement and Concrete Research 33 (7) (2003) 1063–1070.
[9] K.L. Scrivener, Backscattered electron imaging of cementitious microstructures: understanding and quantification, Cement & Concrete Composites 26 (8) (2004) 935–945.
[10] I.G. Richardson, Tobermorite/jennite- and tobermorite/calcium hydroxide-based models for the structure of C–S–H: applicability to hardened pastes of tricalcium silicate, β-dicalcium silicate, Portland cement, and blends of Portland cement with blast-furnace slag, metakaolin, or silica fume, Cement and Concrete Research 34 (9) (2004) 1733–1777.
[11] R. Taylor, I.G. Richardson, R.M.D. Brydson, Nature of C–S–H in 20 year old neat ordinary Portland cement and 10% Portland cement–90% ground granulated blast furnace slag pastes, Advances in Applied Ceramics 106 (6) (2007) 294–301.
[12] R. Berliner, M. Popovici, K.W. Herwig, M. Berliner, H.M. Jennings, J.J. Thomas, Quasielastic neutron scattering study of the effect of water-to-cement ratio on the hydration kinetics of tricalcium silicate, Cement and Concrete Research 28 (2) (1998) 231–243.
[13] B. Pichler, Ch. Hellmich, J. Eberhardsteiner, Spherical and acicular representation of hydrates in a micromechanical model for cement paste—prediction of early-age elasticity and strength, Acta Mechanica 203 (3–4) (2009) 137–162.
[14] B. Pichler, S. Scheiner, Ch. Hellmich, From micron-sized needle-shaped hydrates to meter-sized shotcrete tunnel shells: micromechanical upscaling of stiffness and strength of hydrating shotcrete, Acta Geotechnica 3 (4) (2008) 273–294.
[15] J.M. Taplin, A method of following the hydration reaction in Portland cement paste, Australian Journal of Applied Science 10 (3) (1959) 329–345.
[16] European Committee for Standardization, European Standard EN 196-1: Methods of Testing Cement—Part 1: Determination of Strength, 2005.
[17] R. Hill, Elastic properties of reinforced solids, Journal of the Mechanics and Physics of Solids 11 (5) (1963) 357–372.
[18] P.M. Suquet, Continuum Micromechanics, Volume 377 of CISM Courses and Lectures, Springer Verlag, Wien New York, 1997.
[19] A. Zaoui, Structural Morphology and Constitutive Behavior of Microheterogeneous Materials, in: P. Suquet (Ed.), Continuum Micromechanics, Springer, Vienna, 1997, pp. 291–347.
[20] A. Zaoui, Continuum micromechanics: survey, Journal of Engineering Mechanics (ASCE) 128 (8) (2002) 808–816.
[21] W.R. Drugan, J.R. Willis, A micromechanics-based nonlocal constitutive equation and estimates of representative volume element size for elastic composites, Journal of the Mechanics and Physics of Solids 44 (4) (1996) 497–524.
[22] A. Fritsch, C. Hellmich, Universal microstructural patterns in cortical and trabecular, extracellular and extravascular bone materials: micromechanics-based prediction of anisotropic elasticity, Journal of Theoretical Biology 244 (4) (2007) 597–620.
[23] Z. Hashin, Analysis of composite materials—a survey, Journal of Applied Mechanics 50 (3) (1983) 481–505.
[24] J.D. Eshelby, The determination of the elastic field of an ellipsoidal inclusion, and related problems, Proceedings of the Royal Society of London. Series A 241 (1957) 376–396.
[25] N. Laws, The determination of stress and strain concentrations at an ellipsoidal inclusion in an anisotropic material, Journal of Elasticity 7 (1) (1977) 91–97.
[26] Y. Benveniste, A new approach to the application of Mori–Tanaka's theory in composite materials, Mechanics of Materials 6 (2) (1987) 147–157.
[27] A. Fritsch, L. Dormieux, C. Hellmich, J. Sanahuja, Mechanical behavior of hydroxyapatite biomaterials: an experimentally validated micromechanical model for elasticity and strength, Journal of Biomedical Materials Research. Part A 88 (1) (2009) 149–161.

[28] J. Sanahuja, L. Dormieux, S. Meille, C. Hellmich, A. Fritsch, Micromechanical explanation of elasticity and strength of gypsum: from elongated anisotropic crystals to isotropic porous polycrystals, Journal of Engineering Mechanics 136 (2) (2010) 239–253.
[29] W. Kreher, Residual stresses and stored elastic energy of composites and polycrystals, Journal of the Mechanics and Physics of Solids 38 (1) (1990) 115–128.
[30] L. Dormieux, A. Molinari, D. Kondo, Micromechanical approach to the behavior of poroelastic materials, Journal of the Mechanics and Physics of Solids 50 (10) (2002) 2203–2231.
[31] O. Bernard, F.-J. Ulm, E. Lemarchand, A multiscale micromechanics-hydration model for the early-age elastic properties of cement-based materials, Cement and Concrete Research 33 (9) (2003) 1293–1309.
[32] A.V. Hershey, The elasticity of an isotropic aggregate of anisotropic cubic crystals, Journal of Applied Mechanics (ASME) 21 (1954) 226–240.
[33] E. Kröner, Computation of the elastic constants of a polycrystal based on the constants of the single crystal, Zeitschrift fur Physik. A: Hadrons and Nuclei 151 (4) (1958) 504–518, In German.
[34] R. Hill, A self-consistent mechanics of composite materials, Journal of the Mechanics and Physics of Solids 13 (4) (1965) 213–222.
[35] B. Budiansky, On the elastic moduli of some heterogeneous materials, Journal of the Mechanics and Physics of Solids 13 (4) (1965) 223–227.
[36] T. Mori, K. Tanaka, Average stress in matrix and average elastic energy of materials with misfitting inclusions, Acta Metallurgica 21 (5) (1973) 571–574.
[37] T.C. Powers, T.L. Brownyard, Studies of the physical properties of hardened portland cement paste, Research Laboratories of the Portland Cement Association Bulletin 22 (1948) 101–992.
[38] P. Acker, Micromechanical Analysis of Creep and Shrinkage Mechanisms, in: F.-J. Ulm, Z.P. Bažant, F.H. Wittmann (Eds.), Creep, Shrinkage and Durability Mechanics of Concrete and other Quasi-brittle Materials, 6th International Conference CONCREEP@MIT, Elsevier, Amsterdam, 2001, pp. 15–26.
[39] Ch. Hellmich, H.A. Mang, Shotcrete elasticity revisited in the framework of continuum micromechanics: from submicron to meter level, Journal of Materials in Civil Engineering (ASCE) 17 (3) (2005) 246–256.
[40] G. Constantinides, F.-J. Ulm, The effect of two types of C–S–H on the elasticity of cement-based materials: results from nanoindentation and micromechanical modeling, Cement and Concrete Research 34 (1) (2004) 67–80.
[41] J.D. Bass, Elasticity of Minerals, Glasses, and Melts, Mineral Physics and Crystallography: A Handbook of Physical Constants, American Geophysical Union, 1995, pp. 45–63.
[42] R.A. Helmuth, D.H. Turk, Elastic Moduli of Hardened Portland Cement and Tricalcium Silicate Pastes: Effect of Porosity, Symposium on Structure of Portland Cement Paste and Concrete, vol. 90, Highway Research Board, Washington, DC, 1966, pp. 135–144.
[43] J. Sanahuja, L. Dormieux, G. Chanvillard, Modelling elasticity of a hydrating cement paste, Cement and Concrete Research 37 (10) (2007) 1427–1439.
[44] J. Byfors, Plain Concrete at Early Ages, Technical Report, Swedish Cement and Concrete Research Institute, Stockholm, Sweden, 1980.
[45] C. Hua, A. Ehrlacher, P. Acker, Analyses and models of the autogenous shrinkage of hardening cement paste II. Modelling at scale of hydrating grains, Cement and Concrete Research 27 (2) (1997) 245–258.
[46] L. Stefan, F. Benboudjema, J.-M. Torrenti, B. Bissonnette, Prediction of elastic properties of cement pastes at early ages, Computational Materials Science 47 (3) (2010) 775–784.
[47] V. Smilauer, Z. Bittnar, Microstructure-based micromechanical prediction of elastic properties in hydrating cement paste, Cement and Concrete Research 36 (9) (2006) 1708–1718.
[48] S. Ghabezloo, Association of macroscopic laboratory testing and micromechanics modelling for the evaluation of the poroelastic parameters of a hardened cement paste, Cement and Concrete Research 40 (8) (2010) 1197–1210.
[49] M. Vandamme, F.-J. Ulm, P. Fonollosa, Nanogranular packing of C–S–H at substochiometric conditions, Cement and Concrete Research 40 (1) (2010) 14–26.
[50] J.J. Chen, L. Sorelli, M. Vandamme, F.-J. Ulm, G. Chanvillard, A coupled nanoindentation/SEM-EDS study on low water/cement ratio Portland cement paste: evidence for C–S–H/$Ca(OH)_2$ nanocomposites, Journal of the American Ceramic Society 93 (5) (2010) 1484–1493.
[51] O. Bernard, F.-J. Ulm, J.T. Germaine, Volume and deviator creep of calcium-leached cement-based materials, Cement and Concrete Research 33 (8) (2003) 1127–1136.
[52] F.P. Ganneau, G. Constantinides, F.-J. Ulm, Dual-indentation technique for the assessment of strength properties of cohesive-frictional materials, International Journal of Solids and Structures 43 (6) (2006) 1727–1745.
[53] G. Constantinides, F.-J. Ulm, The nanogranular nature of C–S–H, Journal of the Mechanics and Physics of Solids 55 (1) (2007) 64–90.
[54] R.J.-M. Pellenq, A. Kushima, R. Shahsavari, K.J. Van Vliet, M.J. Buehler, S. Yip, F.-J. Ulm, A realistic molecular model of cement hydrates, Proceedings of the National Academy of Sciences of the United States of America 106 (38) (2009) 16102–16107.
[55] K. Popper, Logic of Scientific Discovery, Springer, Wien, Austria, 1934, In German.
[56] Z.P. Bažant, S.-D. Pang, Mechanics-based statistics of failure risk of quasibrittle structures and size effect on safety factors, Proceedings of the National Academy of Sciences of the United States of America 103 (25) (2006) 9434–9439.
[57] L. Dormieux, D. Kondo, F.-J. Ulm, Microporomechanics, John Wiley & Sons, 2006.
[58] B. Pichler, L. Dormieux, Cracking risk of partially saturated porous media—part I: microporoelasticity model, International Journal for Numerical and Analytical Methods in Geomechanics 34 (2) (2010) 135–157.
[59] B. Pichler, L. Dormieux, Cracking risk of partially saturated porous media—part II: application to drying shrinkage, International Journal for Numerical and Analytical Methods in Geomechanics 34 (2) (2010).